PCCP

PAPER

Enhancing the electrocatalytic activity of 2H-WS$_2$ for hydrogen evolution *via* defect engineering†

Longfei Wu, [a] Arno J. F. van Hoof, [a] Nelson Y. Dzade, [b] Lu Gao, [a] Marie-Ingrid Richard, [cd] Heiner Friedrich, [e] Nora H. De Leeuw, [b] Emiel J. M. Hensen [a] and Jan P. Hofmann [*a]

Transition metal dichalcogenides (TMDs), such as MoS$_2$ and WS$_2$, are promising alternative non-noble metal catalysts to drive the electrocatalytic H$_2$ evolution reaction (HER). However, their catalytic performance is inherently limited by the small number of active sites as well as their poor electrical conductivity. Here, we grow vertically aligned 2H-WS$_2$ on different substrates to expose their edge sites for the HER and introduce a scalable approach to tune these active sites *via* defect engineering. In a thermal hydrogen treatment procedure, sulfur vacancies and metallic tungsten nanoparticles are formed. The extent of desulfurization, and thus the HER activity, can be tuned *via* controlling the H$_2$ annealing conditions. The obtained W/WS$_{2-x}$ electrocatalysts are evaluated experimentally and theoretically to arrive at a better understanding of how to modify the inherently inert 2H-WS$_2$ for more efficient HER.

Introduction

The growing demand for energy has stimulated global efforts to explore renewable energy sources such as wind and solar. However, efficient energy storage to solve the issue of their intermittency remains to be solved.[1–4] Hydrogen is arguably the most promising alternative fuel due to its cleanness, renewability, and high gravimetric energy density.[5] Hydrogen production *via* electrochemical water splitting (hydrogen evolution reaction, HER) has been emerging as a promising sustainable approach.[6] The key challenge for enabling this process at a large scale is the development of efficient, durable and low cost electrocatalysts for HER. Currently, platinum-based materials serve as the benchmark catalysts for HER due to their high catalytic activity;[7] yet, the scarcity and cost of Pt significantly hamper their widespread application.[2,8] Transition metal

dichalcogenides (TMDs) with two-dimensional (2D)-layered crystal structures, such as MoS$_2$ and WS$_2$, have been extensively used as HER catalysts.[9] Both experimental[6] and computational[10] studies show comparable catalytic activity with commercial Pt/C composites, as such potentially rivalling state-of-the-art catalysts in electrochemical or photoelectrochemical cells.[9,11]

Although the (0001) basal planes of semiconductor phase TMDs (2H-TMDs) are not active HER catalysts, the edge sites of 2H-TMDs were theoretically predicted[12] and experimentally[13] verified to be active for HER. Many efforts have been devoted to maximally expose those edge sites by various methods such as nano-structuring,[13] size-controlling,[14] and defect engineering.[15,16] However, the guiding principle for all these approaches usually has been to optimize the active sites rather than tailor the inert basal planes because the edge sites have been identified to be HER active exhibiting a similar Gibbs free energy for atomic hydrogen adsorption (ΔG_{H}) as the most active Pt-group metals.[17] Specifically for MoS$_2$, extensive efforts have been devoted in developing feasible ways for engineering higher densities of active sites.[18] As to the edge sites of 2H-TMDs, only pure metal edges or metal edges passivated with S-monomers are preferably favorable for HER, whereas the configuration with full S-passivation (S-dimers) is too inert for these relevant catalytic reactions to occur.[19,20] Thus, active sites can be created on either the (0001) basal plane of 2H-TMDs or at the inert S-dimer edges. Tsai and co-workers demonstrate an electrochemical process for generating S-vacancies in monolayer and polycrystalline MoS$_2$ to tune the HER activity.[21] Cheng *et al.* reported a remote hydrogen-plasma process to create sulfur vacancies on the

^{a} *Laboratory for Inorganic Materials and Catalysis, Department of Chemical Engineering and Chemistry, Eindhoven University of Technology, P.O. Box 513, 5600 MB Eindhoven, The Netherlands. E-mail: J.P.Hofmann@tue.nl*

^{b} *Faculty of Geosciences, Utrecht University, P.O. Box 80.021, 3508 TA Utrecht, The Netherlands*

^{c} *Aix Marseille Université, CNRS, Université de Toulon, IM2NP UMR 7334, 13397 Marseille, France*

^{d} *ID01/ESRF, The European Synchrotron, 71 rue des Martyrs, 38043 Cedex Grenoble, France*

^{e} *Laboratory of Materials and Interface Chemistry, Department of Chemical Engineering and Chemistry, Eindhoven University of Technology, P.O. Box 513, 5600 MB Eindhoven, The Netherlands*

† Electronic supplementary information (ESI) available: Experimental details and additional characterization. See DOI: 10.1039/c9cp00722a

This journal is © the Owner Societies 2019

Phys. Chem. Chem. Phys., 2019, **21**, 6071–6079 | 6071

basal plane of monolayer crystalline TMDs while maintaining the pristine morphology and structure.[22] Aside from desulfurization, other studies report on maximizing the number of exposed active metal sites to achieve an enhancement for HER activity. Woods et al.[23] and Wang et al.[24] present a unique vertically aligned MoS_2 and MoS_2/WS_2 structure with exposed metal edge sites which show notable HER activity. This prominent improvement in activity was ascribed to the distinct vertical structure maximizing the exposure of catalytically active sites. Other approaches such as thermal annealing[25] or ball milling[26] were also applied to tune the HER activity of TMDs. However, even though a lot of efforts have been devoted to developing versatile methods to tune the structure of 2H-TMDs and to increase the number of HER active sites, deeper understanding of the structural evolution during treatment (for instance, texturization[25] and desulfurization[26]) processes and how to correlate structural changes to HER activity needs to be developed.

Here, we have selected WS_2 as a platform to induce more active HER sites in the 2H phase via a controllable and effective thermal H_2 treatment procedure. Vertically aligned 2H-WS_2 was grown on various substrates (SiO_2/Si, Si_3N_4 and carbon fiber paper) using sulfurization of sputter-deposited metal tungsten. By annealing in a hydrogen atmosphere, sulfur vacancies and tungsten nanoparticles were formed which are supposed to act as active sites for HER. Further hydrogen treatment yielded a highly defective tungsten sulfide (WS_{2-x}). In addition, extended H_2 annealing led to a complete change of the initial structure and emergence of new morphologies such as nanotubes and porous structures. The as-derived highly defective WS_{2-x} shows prominent HER activity compared to the pristine 2H-WS_2 and reported tungsten sulfide materials in the literature. A detailed nanostructure analysis has been conducted on the highly defective WS_{2-x}, applying XPS, HR-TEM, HAADF-STEM and synchrotron-based nano-focus XRD to shed light on the observed significant improvement in HER activity.

Experimental

Materials synthesis

2H-WS_2 films were prepared via sulfurization of sputtered metal tungsten on different substrates in a thermal chemical vapor deposition (CVD) system (Fig. S1, ESI†).[27] Specifically, SiO_2 (300 nm)/Si sputter-coated with 20 nm W was placed at the center of a tube furnace. After loading 500 mg (99.98%, Aldrich) sulfur powder at the upstream, the tube was sealed, evacuated and refilled with N_2 three times to remove O_2 in the system. Then, the tube was flowed with Ar (100 sccm) for 15 min. Afterwards, the furnace was heated up with a heating rate of 20 °C min^{-1} and kept for 15 min at the target temperature (600 °C). The sulfur powder was heated to 170 °C accordingly. Defective tungsten sulfide was prepared by a post-synthetic treatment under similar conditions. The sulfur source was cooled down and subsequently H_2 with certain flow rate was introduced at the target temperature. Samples for transmission

electron microscopy (TEM) analysis were prepared on custom-made TEM grids (Lionix BV) which consist of a silicon frame and a central part that was etched away to create a 15–20 nm thick silicon nitride membrane window (100×100 μm^2) where the electron beam can pass.[28–31] Prior to tungsten sputtering, the TEM grids were calcined in dry air to form a 3 nm thick surface layer of silicon oxide.[28]

Characterization

X-ray photoelectron spectroscopy (XPS) was recorded on a Thermo Scientific K-Alpha instrument equipped with a monochromatic X-ray source ($h\nu$(Al Kα) = 1486.6 eV). Binding energy calibration was performed by using the sp^3 C 1s peak of adventitious carbon at 284.6 eV as reference. Spectra were fitted by Casa XPS software. Raman spectra measurements were performed on a Renishaw Raman InVia microscope equipped with a 514 nm laser, integrated switchable gratings with 600 or 1800 lines per mm, and a CCD detector. For each scan, 5 accumulations with acquisition time of 10 s were taken. TEM images were acquired with a FEI Tecnai 20 transmission electron microscope equipped with a LaB$_6$ filament and operated at an acceleration voltage of 200 kV. High resolution TEM (HR-TEM) and high angle annular dark field scanning transmission electron microscopy (HAADF-STEM) imaging were performed at room temperature on a FEI CryoTitan transmission electron microscope which is equipped with a field emission electron gun and operated at 300 kV. HR-TEM and select area electron diffraction (SAED) images were acquired using a Gatan 2K CCD camera. STEM images were acquired using a probe convergence angle of 10 mrad, a dwell time of 2 μs and a camera length of 115 mm in combination with a Fischione HAADF detector. Nano X-ray diffraction analysis was performed at the European Synchrotron (ESRF) at the ID01 X-ray diffraction and scattering beamline with beam energy of 8.0 keV and beam size of 100×400 nm^2. Energy dispersive X-ray spectroscopy (EDX) was obtained on a Phenom ProX scanning electron microscope with 5 kV acceleration voltage. Grazing incidence X-ray diffraction (GI-XRD) measurement was performed on a Panalytical X Pert PRO MRD employing Cu Kα (1.54 Å) radiation with an incidence angle of 0.5° with respect to the substrate plane. Near Ambient Pressure XPS (NAP-XPS) was conducted on a SPECS system with a PHOIBOS 150 NAP hemispherical energy analyzer in 5 mbar H_2 pressure at 600 °C.

Electrochemical measurements

Electrochemical measurements were performed in a three-electrode electrochemical cell with saturated calomel electrode (SCE) (0.269 V vs. reversible hydrogen electrode (RHE)) as the reference electrode, Pt foil (1×2 cm^2) as the counter electrode, and 0.5 M H_2SO_4 (99.999%, Sigma-Aldrich) as electrolyte. The electrolyte was prepared with 18 MΩ cm deionized Milli-Q water and purged with Ar for 20 min to remove O_2 in the solution prior to the measurements. Cyclic voltammetry and linear sweep voltammetry curves were recorded on a Metrohm Autolab PGSTAT302N potentiostat, and current density values are normalized by geometric area. IR correction has been done

6072 | Phys. Chem. Chem. Phys., 2019, 21, 6071–6079

This journal is © the Owner Societies 2019

before normalization on geometric area. AC electrochemical impedance spectroscopy (amplitude: 10 mV) was recorded at open circuit potential (OCP) in the frequency range of 100 kHz to 1 Hz. Stability tests were conducted by recording chrono-potentiostatic responses with glassy carbon as a counter electrode to exclude possible contamination by Pt.

Results and discussion

Reduced WS_{2-x} as catalyst for HER

The synthesis method to prepare defective tungsten sulfide is schematically depicted in Fig. 1a. Elemental W films (20 nm) were deposited on a SiO_2 (300 nm)/Si ((100) orientation, type: P/B, resistivity: 0–100 Ohm cm) substrate by magnetron sputtering, then reacted with sulfur, as described in the experimental section to produce WS_2. Fig. 1b shows a typical TEM image of a WS_2 film revealing the presence of vertically aligned layers with an inter-layer spacing of ~ 0.67 nm.[32] Grazing-incidence X-ray diffraction (Fig. S2, ESI†) indicates a strong peak at $2\theta = 14.12°$ which corresponds to the (002) reflection (interlayer spacing = 0.67 nm) of the semiconducting 2H phase of $WS_{2.32}$.[33] The as-prepared 2H-WS_2 was annealed at 600 °C with 10% H_2 concentration (total flow: 100 sccm, Ar as balance) for 6 h to remove sulfur atoms and produce metal sites or clusters.
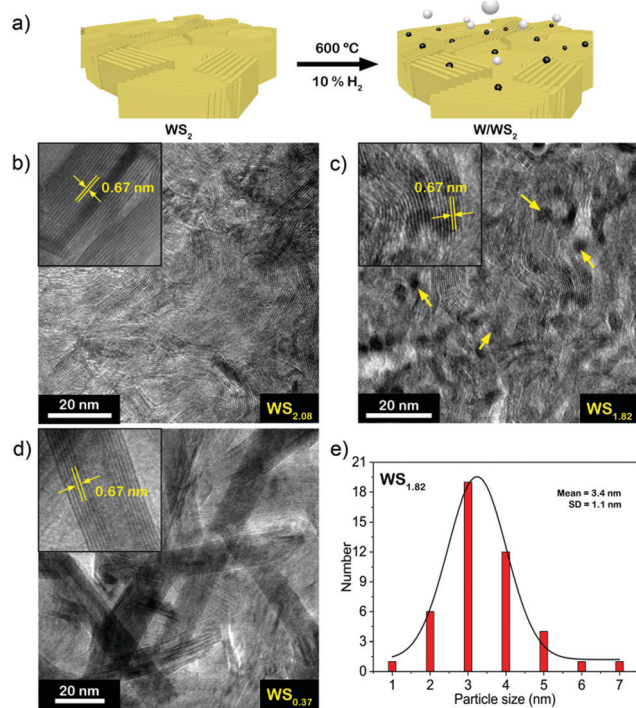

Fig. 1 (a) Scheme showing the transformation of WS_2 to W/WS_{2-x} upon annealing in H_2 atmosphere; (b) TEM images of pristine $WS_{2.08}$, inset: lattice spacing obtained from HRTEM; (c) TEM image of $WS_{1.82}$ obtained via annealing in 10% H_2 at 600 °C for 6 h, arrows indicate the formation of nanoparticles, inset: lattice spacing obtained from HRTEM; (d) TEM image of $WS_{0.37}$ obtained via H_2 annealing (10%) at 600 °C for 10 h, inset: lattice spacing obtained from HRTEM; (e) size distribution of W nanoparticles for $WS_{1.82}$ obtained from the TEM image shown in (c).
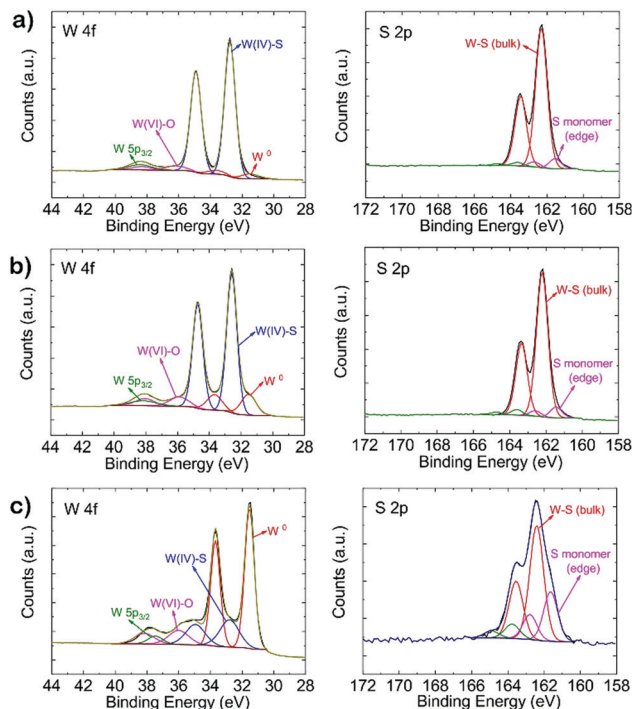

Fig. 2 W 4f and S 2p XP spectra of pristine $WS_{2.08}$ (a), $WS_{1.82}$ (b) and $WS_{0.37}$ (c).

The TEM image in Fig. 1c shows that nanoparticles with an average size of 3 nm were formed on the film along with an overall sulfur/tungsten (S/W) ratio of 1.82 as obtained by X-ray photoelectron spectroscopy (XPS, Fig. 2). Interestingly, when we further prolonged the H_2 annealing time to 10 h, the initial vertical structure turned into new structures such as multi-walled WS_{2-x} nanotubes (lattice spacing: 0.67 nm) with an outer diameter of 10–17 nm (Fig. 1d and Fig. S4, ESI†),[34–36] along with a decrease of the S/W ratio to 0.37.

A detailed XPS analysis of the different tungsten sulfide samples is shown in Fig. 2. The W 4f spectrum can be deconvoluted into four components. The peak at 38.6 eV corresponds to W $5p_{3/2}$. Two characteristic peaks of WS_2 centered at 32.7 eV (W $4f_{7/2}$) and 34.9 eV (W $4f_{5/2}$) are observed, while the high binding energy peak at 36.1 eV corresponds to the W $4f_{7/2}$ component of WO_3 which might be due to a slight oxidation of the films resulting from sample handling in air.[14,37,38] Aside from the decreasing S/W ratio, the obvious increase of the W $4f_{7/2}$ peak at 31.4 eV demonstrates that metallic phase W^0 has been produced. This is substantiated by the S 2p XP spectra. Here, except for the main doublet centered at binding energies of 162.3 and 163.4 eV corresponding to the S $2p_{3/2}$ and S $2p_{1/2}$ components of WS_2, respectively, the increase of sulfur monomer (edge) species at 161.5 eV ($2p_{3/2}$) and 162.6 eV ($2p_{1/2}$) also indicates that more W–S (bulk) bonds were broken generating more sulfur monomers.[19] To assess the progressing reduction of WS_2, we applied Near Ambient Pressure (NAP)-XPS to monitor in situ changes in S and W speciation during annealing in a H_2 atmosphere. Fig. S3 (ESI†) shows that the S/W ratio decreases
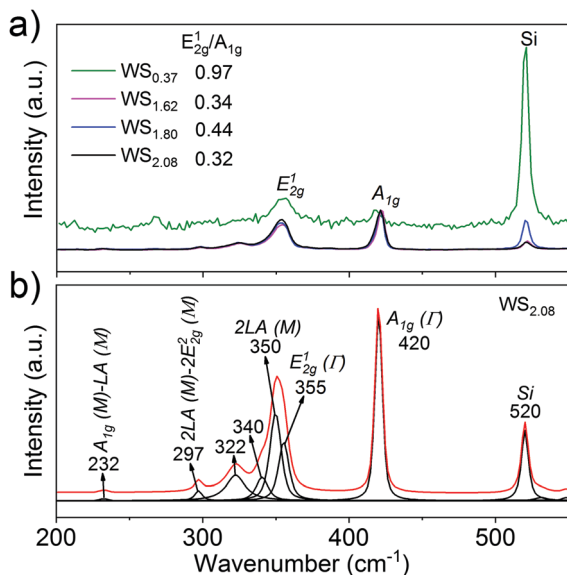
Fig. 3 (a) Raman spectra (normalized on the A_{1g} peak) of tungsten sulfide films prepared on SiO_2/Si substrates; (b) fitted (Gaussian–Lorentzian) spectra of $WS_{2.08}$.

Fig. 4 (a) Linear sweep voltammetry curves of tungsten sulfide obtained with different S/W ratios in 0.5 M H_2SO_4. Scan rate: 5 mV s^{-1}. (b) Tafel slopes obtained from LSV curves in (a).

from 2.89 to 1.91 within two hours of H_2 treatment at 600 °C under 5 mbar H_2 pressure.

The as-prepared vertically aligned and defective tungsten sulfide is further characterized by Raman spectroscopy.[39] Fig. 3 shows the normalized Raman spectra of tungsten sulfide with stoichiometric ratio ($WS_{2.08}$), treated with H_2 annealing ($WS_{1.80}$, $WS_{1.62}$), and highly defective $WS_{0.37}$ after prolonged hydrogen treatment. The peaks at ∼355 and 420 cm^{-1} are assigned to the first-order modes at the Brillouin zone center of E^2_{2g} (Γ) (in plane vibration phonon mode) and A_{1g} (Γ) (out-of-plane vibration phonon mode) of 2H-WS_2 respectively.[32]

Other small features at ∼297 and ∼232 cm^{-1} are assigned to the second longitudinal acoustic mode (2LA (M)) of 2 E^2_{2g} and A_{1g} (M)–LA (M) respectively, which are consistent with those observed in the literature.[32,40–42] One unique feature observed in our Raman spectra is that the intensity ratio of E^1_{2g}/A_{1g} is below unity for stoichiometric and less defective tungsten sulfide, which indicates a prominent out-of-plane vibration (A_{1g}) over the in-plane vibration (E^1_{2g}) mode. The small E^1_{2g}/A_{1g} ratio indicates a more pronounced presence of vertically aligned layers which is consistent with the TEM results in Fig. 1b.[31,39,41] However, for highly defective tungsten sulfide ($WS_{0.37}$), the Raman intensity of the material was significantly weakened along with an increase of the E^1_{2g}/A_{1g} ratio to 0.97. The former indicates that the crystallinity of the tungsten sulfide films has decreased, while the latter points to a progressing loss of vertical alignment under the applied harsh reduction conditions.

The as-prepared tungsten sulfide films were investigated as electrocatalysts for HER in a standard three-electrode electrochemical cell in 0.5 M H_2SO_4 electrolyte. Fig. 4 displays the linear sweep voltammetry (LSV) curves of tungsten sulfide films with various S/W ratios. With decreasing S/W ratio, the LSV
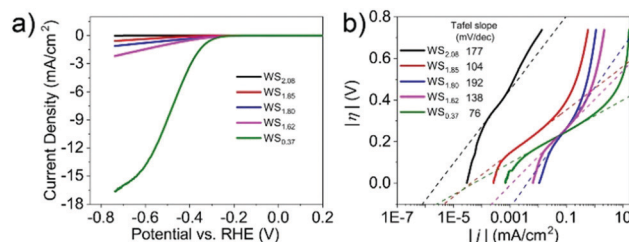
curves demonstrate higher current density and the Tafel slope decrease accordingly, which means that the increase of sulfur vacancies and the presence of metal sites contribute to the improvement of HER activity. Despite the increase of tungsten oxide species detected by XPS with decreasing S/W ratio, we do not observe any notable reduction peaks in the CV curves (Fig. S7, ESI†), which suggests that the defective tungsten sulfide films are stable in acid media.[38]

To further investigate the local crystal structure and phase composition of defective tungsten sulfide, TEM images with corresponding selected area electron diffraction (SAED) patterns as well as HAADF-STEM are displayed for $WS_{0.95}$ in Fig. 5. This sample was directly prepared on a TEM grid and annealed at 600 °C with 10% H_2, where a and b represent two typical regions on the grid. In Fig. 5a and b, the TEM image of (a1) shows that the majority of the vertically aligned layered structure is well maintained except for some nanoparticles, which can be either metal
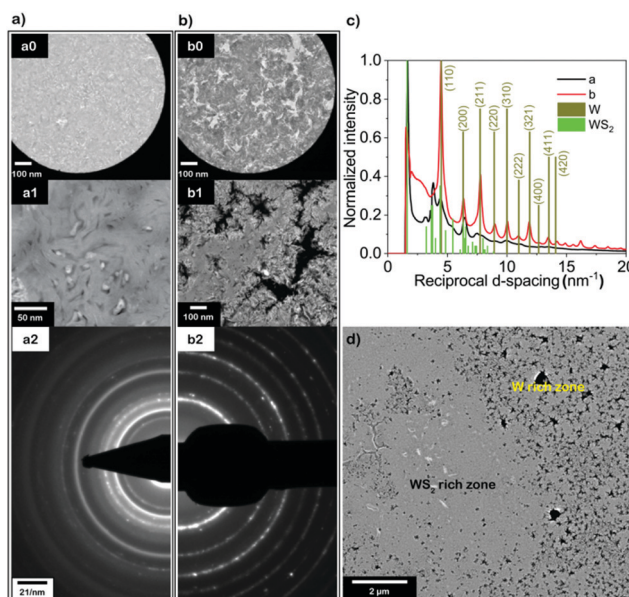

Fig. 5 (a and b) Selected area bright field TEM (BF-TEM) images (a0 and b0) and HAADF-STEM images (a1 and b1) of $WS_{0.95}$, (a) and (b) corresponding to different regions of the sample, typical selected area electron diffraction (SAED) patterns of (a1) and (b1) are shown in (a2) and (b2), respectively; (c) radially averaged SAED signal for (a1) (black curve) and (b1) (red curve); (d) low magnification STEM image of $WS_{0.95}$.

6074 | *Phys. Chem. Chem. Phys.*, 2019, **21**, 6071–6079

This journal is © the Owner Societies 2019

W or sulfur as residue from the sulfurization process; (b0) and (b1) display a region where most of the aligned lamellar structure is destroyed and a lot of holes and pits on a sub-μm scale have appeared (bright in BF-TEM (a0, b0), dark in HAADF-STEM (a1, b1)) across the film. The significant morphological difference in these two regions of the same sample led us to further investigate their crystal structures. The appearance of rings in the SAED patterns indicates the presence of multiple crystalline orientations with respect to the electron beam within the probed area, highlighting the polycrystalline nature of the regions a1 and b1 (Fig. 5). The radial average of the SAED patterns obtained in both regions is plotted in Fig. 5c. For comparison, standard diffraction data for W (dark yellow, JCPDS card number: 01-1203) and WS_2 (green, JCPDS card number: 08-0237) are included. Interestingly, both W and WS_2 are present (Fig. 5c) in regions a and b, while region a has less W content compared to that of region b based on W(110), (211), (310) *etc.* At lower magnifications in STEM, the defective tungsten sulfide can be clearly divided into a WS_2-rich and W-rich zone, respectively, which can be a result of non-uniformity across the film during the H_2 treatment process. Moreover, we conducted synchrotron-based nano-focus X-ray diffraction to examine the local crystal structure in small sample areas. The co-existence of W and WS_2 on a sub-μm scale (100×400 nm^2) is evident; results are shown in Fig. S15 (ESI†), where clear W(110) reflections at $2\theta = 40.2°$ could be observed next to reflections of WS_2. In order to complete the microstructural analysis, we have conducted SEM and EDX mapping measurements to check the morphology and distribution of elements on the μm scale. The pinholes (dark regions) shown in SEM images obtained with a back-scattered electron detector (BSE) (Fig. S16a, ESI†) are caused by nano-structuring during the H_2 treatment process. The merged EDX mapping of O and S indicates that there is a slight oxidation of the film.

Comparison with metallic W

We also compared HER activities of the highly defective tungsten sulfide ($WS_{0.37}$) with sputtered metallic tungsten (Fig. S5, ESI†). Remarkably, $WS_{0.37}$ shows both lower onset potential and much higher current density than those of sputtered W. The enhanced HER activity is further illustrated by comparing the Tafel slopes (Fig. S5d, ESI†), where $WS_{0.37}$ exhibits a smaller value of 77 mV per decade (without uncompensated resistance correction) as compared to sputtered W (145 mV per decade). Additionally, Nyquist plots shown in Fig. S5c (ESI†) indicate that the impedance of W is almost three times higher than that of $WS_{0.37}$ (83 Ω for W and 32 Ω for $WS_{0.37}$), which is ascribed to the serious surface oxidation of sputtered W (Fig. S6, ESI†). The earlier onset of catalytic activity and lower Tafel slope of highly defective tungsten sulfide suggest that the free binding energy of hydrogen to $WS_{0.37}$ is much closer to equilibrium than stoichiometric WS_2 and metallic W.

Influence of H_2 annealing temperature

To evaluate the influence of annealing temperature on the structure and activity change of 2H-WS_2, we treat the as-prepared films at 700 °C in 10% H_2 for different time. Fig. S8 (ESI†) shows the XP spectra of defective tungsten sulfide obtained at 700 °C indicating that the S/W ratio decreases from 2.07 to 1.18 after 1.5 h H_2 treatment and further decreases to 0.17 after 3 h. As mentioned before, the presence of sulfur monomer (edge) species at BE(S $2p_{3/2}$) = 161.5 eV is an indication of the breaking of W–S (bulk) bonds. The increasing proportion of this kind of sulfur bond further evidences the generation of more defect sites. The morphology of defective tungsten sulfide prepared at 700 °C was also studied by TEM shown in Fig. S9 (ESI†). The vertically aligned layered WS_2 evolves into an irregular defect-rich structure with long tubes after 1 h H_2 treatment at 700 °C, whereas the tubes disappear and more defects are generated with longer annealing time. Further Raman characterization (Fig. S10, ESI†) shows that the intensity of the E^1_{2g} and A_{1g} peaks gradually decreases with increasing H_2 annealing time, which is further evidence of the increasing loss of crystallinity. Electrochemical tests were performed on the aforementioned tungsten sulfide films to evaluate their HER activity. The CV and LSV curves in Fig. S11 (ESI†) demonstrate a dramatic increase of the current density and lower onset potential for films treated at 700 °C in 10% H_2 for 0.5 to 3 h compared with pristine WS_2. Surprisingly, further extension of H_2 annealing at 700 °C to 6 h shows a much lower HER activity compared with H_2 treatment for 3 h. Such a trend is also reflected in impedance spectra shown in Fig. S11d (ESI†), where a larger uncompensated resistance value is observed for 6 h.

Under even higher annealing temperature of 850 °C, the S/W ratio sharply decreases to 0.16 even with 5% H_2 after 3 h. No further decrease of S/W ratio could be observed even if we prolong the annealing time to 6 or 10 h as shown in Fig. S12 (ESI†). The influence of high temperature annealing on the crystal structure is also reflected in Raman spectra (Fig. S13, ESI†), which show no obvious Raman features of WS_2 upon annealing at 850 °C in H_2 (5%) atmosphere for 3 h. Hydrogen evolution activity tests in Fig. S14 (ESI†) show that $WS_{0.16}$ exhibits much higher activity than pristine, stoichiometric WS_2. However, extended exposure to H_2 at 850 °C results in a decrease of current density and an increase of electron transfer resistance, which is consistent with what we observed for defective tungsten sulfide films prepared at 700 °C. Even though for tungsten sulfide films prepared at 600 °C a lower S/W ratio resulted in a higher HER activity, it seems that a higher H_2 annealing temperature together with prolonged treatment time leads to a delamination of the films, thereby hampering the electron transfer process from substrate to catalyst.

Fig. 6 summarizes the comparison of defective tungsten sulfide films prepared at different temperatures. (S)TEM images show that under different annealing temperatures the initial vertically aligned lamella structure turns into highly defective structures with the presence of nanotubes ($WS_{0.37}$, Fig. 6a) and discontinuous flakes ($WS_{0.14}$, Fig. 6c). The electrocatalytic activity towards HER of the as-prepared tungsten sulfide films has also been evaluated (Fig. 6d and e). Both CV and LSV curves exhibit a prominent increase of current density and an earlier onset of catalytic activity. Despite the fact that the smaller S/W ratio suggests that more sulfur vacancies are produced which would
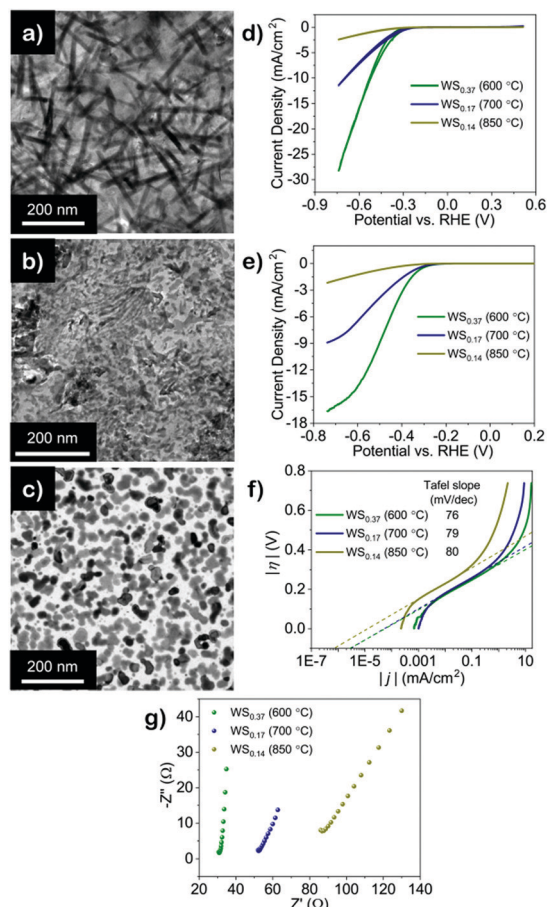
This journal is © the Owner Societies 2019

Phys. Chem. Chem. Phys., 2019, **21**, 6071–6079 | **6075**

Fig. 6 (a–c) TEM images of $WS_{0.37}$ (600 °C) (a), $WS_{0.17}$ (700 °C) (b) and $WS_{0.14}$ (850 °C) (c); cyclic voltammetry (d) and linear sweep voltammetry (e) curves of highly defective tungsten sulfide prepared at different temperatures in 0.5 M H_2SO_4. Scan rate: 50 mV s^{-1} for CV and 5 mV s^{-1} for LSV; (f) Tafel slopes obtained from LSV curves in (e); (g) EIS Nyquist plots of corresponding films collected at open circuit potential in 0.5 M H_2SO_4 electrolyte with an AC amplitude of 10 mV.

contribute to an improved HER activity, the highly defective tungsten sulfides $WS_{0.17}$ and $WS_{0.14}$ have issues such as severe film discontinuities and loss of catalyst material as evidenced by the appearance of Si in the XPS survey spectrum. Electrochemical impedance spectroscopy (EIS) is presented in Fig. 6f to investigate the electrode kinetics under HER conditions. The measurements were carried out from 100 kHz to 1 Hz at open-circuit potential (OCP). The impedance data demonstrate an uncompensated resistance of 31 Ω for $WS_{0.37}$, while tungsten sulfide films annealed at higher temperature present almost two (52 Ω for $WS_{0.17}$) or three (86 Ω for $WS_{0.14}$) times larger values. Besides, the S/W ratio decreases rapidly at high H_2 annealing temperature, which makes it difficult to control the generation of sulfur vacancies and W metal clusters. Therefore, a moderate annealing temperature (*i.e.* 600 °C) is ideal to produce highly defective tungsten sulfide with nanostructures that provide more exposed active sites for hydrogen evolution without slowing down the kinetic processes such as electron or charge transfer in the films.

Electrochemical evaluation of defective WS_{2-x} on porous carbon fiber paper support

To further demonstrate the applicability of the H_2 annealing method to prepare efficient HER catalysts, we have used conductive porous carbon fiber paper (CFP) as substrate. The polarization curves shown in Fig. 7a demonstrate the HER activities of tungsten sulfide with different S/W ratios (XPS shown in Fig. S17, ESI†), which show similar trends for those on SiO_2/Si substrates: the smaller the S/W ratio, the higher the HER activity. The linear portions of the Tafel plots before (solid lines, Fig. 7c) and after uncompensated resistance correction (iR-corrected, dashed lines, Fig. 7c) are fitted to the Tafel equation ($\eta = b \log j + a$, where j is the current density and b is the Tafel slope), yielding Tafel slopes of ~ 73 (without iR correction) or ~ 60 mV per decade (iR-corrected). Typically, a Tafel slope of ~ 120 mV per decade indicates that the rate-limiting step is the Volmer reaction ($H^+ + e^- \rightarrow H_{ads}$) and the rate-limiting step becomes the Heyrovsky reaction ($H_{ads} + H^+ + e^- \rightarrow H_2$) when the Tafel slope is ~ 40 mV per decade.[22] Therefore, the substantially decreased Tafel slope from 152 mV per decade ($WS_{1.97}$) to 60 mV per decade ($WS_{0.44}$) suggests that the HER mechanism on highly defective tungsten sulfide becomes Volmer–Heyrovsky-type with electrochemical desorption of hydrogen as the rate-limiting step.[22,43]

To evaluate the relative differences in electrochemical active surface area of tungsten sulfide with various S/W ratios, we have used cyclic voltammetry (CV). There, we have assumed that the current response recorded in the potential window (0.1–0.2 V *vs.* RHE) with different scan rates (20–180 mV s^{-1}) (Fig. S19, ESI†) is only due to the capacitive charging of the double layer. By drawing the differences between anodic and cathodic current densities ($\Delta j = j_a - j_c$) against the CV scan rates
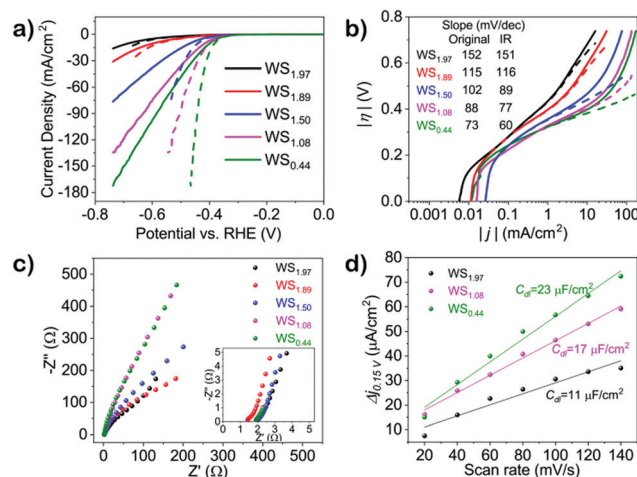

Fig. 7 (a) Linear sweep voltammetry (LSV) curves of WS_{2-x} prepared on carbon fiber paper; dashed lines are obtained after film resistance correction; (b) Tafel slopes for WS_{2-x} obtained from LSV curves in (a); (c) EIS Nyquist plots of corresponding samples collected at open circuit potential with an AC amplitude of 10 mV, inset: zoom-in Nyquist plots; (d) electrochemical double layer capacitance (C_{dl}) of $WS_{1.97}$, $WS_{1.08}$ and $WS_{0.44}$. Electrolyte: 0.5 M H_2SO_4, LSV scan rate: 5 mV s^{-1}.

at a given potential (0.15 V *vs.* RHE), a linear fitting can be conducted from the curve which is shown in Fig. 7d. The significant increase of active sites for highly defective tungsten sulfide is illustrated by the increase of C_{dl} from 11 μF cm^{-2} ($WS_{1.97}$) to 23 μF cm^{-2} ($WS_{0.44}$). Since the significant increase of HER activity far exceeds the increase of surface area, we assume this trend to be related to the intrinsically more active nature of the highly defective tungsten sulfide.

Next to its activity, the stability is a similarly important criterion of a promising electrocatalyst. To evaluate the stability of the as-prepared defective tungsten sulfide, long-duration chronopotentiometric measurements of HER were conducted at a constant current density of 4.45 mA cm^{-2} for $WS_{0.44}$, as shown in Fig. S20 (ESI†). There is a slight decrease of the potential at the beginning which quickly stabilizes and remains constant within ±5 mV until the end of the test after 24 h. XPS sputter depth profiling of $WS_{0.44}$ after HER testing (Fig. S21, ESI†) shows the initial appearance of a sulfate peak and an increase of W(VI)–O peak, which is due to the oxidation of the surface in the electrolyte. However, after 10 cycles (∼20 nm) of Ar$^+$ sputtering, the content of W(VI)–O is similar to fresh samples indicating that oxidation is confined to the topmost surface layers. The highly defective tungsten sulfide film ($WS_{0.44}$) exhibits a low Tafel slope of 54 mV per decade, which compares well with other reported WS_2-based HER catalysts (see Table S1, ESI†).[26,44–47]

DFT modelling of H adsorption on defective WS_{2-x}

To gain atomic-level insight into the enhanced intrinsic HER activity of W/WS_{2-x}, we have performed DFT calculations to investigate the hydrogen adsorption free energies of the defective tungsten sulfides for HER. Firstly, the Gibbs free energies for hydrogen adsorption (ΔG_H) on a stoichiometric WS_2(0001) basal plane (BP) (without sulfur vacancies) and defective BP (with S vacancy site) have been calculated, where ΔG_H shows a much smaller value of +0.17 eV on an S vacancy site compared to +2.33 eV on the perfect BP (Fig. S22, ESI†). However, the positive value of ΔG_H indicates that hydrogen adsorption on both WS_2 BP and defective BP is endothermic and therefore unlikely to occur. As discussed, in the H_2-annealed material, there co-exist a WS_2-rich zone and a W-rich zone where both perfect and defective WS_2 BP are present. Even though XPS analysis shows the presence of W–O species on the surface, former studies indicate that W sites in WO_3 are inert for hydrogen adsorption.[48,49] Also, according to the Pourbaix diagram for the tungsten-water system at 25 °C, the prevailing phase under the applied potential/pH conditions should be W^0.[50] Therefore, we have calculated ΔG_H on a plausible active site model structure in the form of a tetrahedral W_4 cluster supported on either perfect (Fig. 8) or defective (Fig. S23, ESI†) basal planes of $2H$-WS_2. Now, adsorption energies are exothermic and in both cases show a value that is much closer to equilibrium, which indicates that they are HER-active sites.

Additionally, we propose that the creation of W-rich zones through the growth of W-clusters on both the perfect and defective WS_2 BP may impact on the electronic structure and
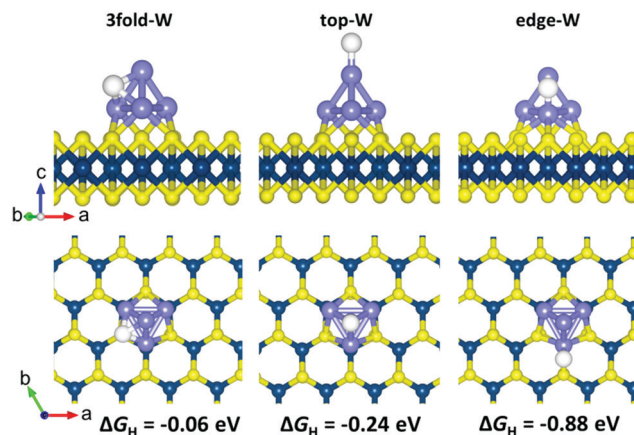

Fig. 8 Calculated Gibbs free energy for hydrogen adsorption on the probable adsorption sites of a tetrahedron W cluster on the perfect WS_2 basal (0001) plane (BP).

improve the intrinsic electronic conductivity of the WS_2 nanosheets. To verify this hypothesis, we have calculated the partial density of states (PDOS) of the perfect WS_2 monolayer and those with a tetrahedral W_4 cluster supported on either the perfect or defective basal planes, as shown in Fig. S24 (ESI†). The results indicate that compared to the perfect WS_2 monolayer bandgap of 1.98 eV, the growth of the W-clusters on the perfect WS_2 monolayer (S/W = 1.72) introduces donor states (intermediate states) in the band gap, whereas W-clusters on the defective WS_2 monolayer (S/W = 1.52) narrow the bandgap to 0.85 eV. Through both the intermediate states and the narrowed bandgap, electrons at the valence band edge can be excited more easily to the conduction band edge, suggesting that the growth of W-clusters could introduce more charge carriers and improve the intrinsic conductivity of the WS_2 material. The enhanced electrical conductivity together with more optimal hydrogen adsorption energies on the W-clusters are primary reasons leading to the enhanced HER activity of the WS_2 materials with lower S/W ratios.

Conclusions

We have presented a versatile method to prepare highly defective tungsten sulfide which exhibits an improved activity in the electrochemical H_2 evolution reaction. We have demonstrated the generality of this method by applying it to WS_2 supported on various substrates (SiO_2/Si, Si_3N_4, and carbon fiber paper). The S/W ratio, and with that the HER activity, can be tuned *via* changing the H_2 annealing temperature, time and H_2 concentration. With decreasing S/W ratio, we succeeded in tuning the amount of S vacancies and W nanoparticles which both are intrinsically more active than the basal planes of WS_2. The increased catalytic activity towards hydrogen evolution has been supported by a low Tafel slope of 60 mV per decade for highly defective tungsten sulfide ($WS_{0.44}$). We presume that the improved HER performance of the highly defective tungsten sulfide films relates to their unique properties which feature

the following advantages: (1) nanostructuring and texturization during H_2 treatment generate more active sites; (2) the intrinsic catalytic activity of the W clusters on either perfect or defective basal planes contributes to the improvement of activity; (3) the presence of metallic W in the defective WS_{2-x} films improves the intrinsic electronic conductivity thus facilitating charge transfer through the films. Our approach does not only provide a fundamental platform to study the role of sulfur vacancies and W content in highly defective WS_{2-x} in the HER, but it is also applicable to a wide range of other transition metal chalcogenides. To arrive at a conclusive understanding of the role of metallic W species in the HER over-defective WS_{2-x}, further studies, ideally under electrochemical *operando* conditions, are needed.

Conflicts of interest

There are no conflicts to declare.

Acknowledgements

References

1 B. Seo, G. Y. Jung, Y. J. Sa, H. Y. Jeong, J. Y. Cheon, J. H. Lee, H. Y. Kim, J. C. Kim, H. S. Shin, S. K. Kwak and S. H. Joo, *ACS Nano*, 2015, **9**, 3728–3739.

2 S. S. Chou, N. Sai, P. Lu, E. N. Coker, S. Liu, K. Artyushkova, T. S. Luk, B. Kaehr and C. J. Brinker, *Nat. Commun.*, 2015, **6**, 8311–8318.

3 A. A. Tedstone, D. J. Lewis and P. O'Brien, *Chem. Mater.*, 2016, **28**, 1965–1974.

4 X. Chia, A. Ambrosi, Z. Sofer, J. Luxa and M. Pumera, *ACS Nano*, 2015, **9**, 5164–5179.

5 J. Hu, B. Huang, C. Zhang, Z. Wang, Y. An, D. Zhou, H. Lin, M. K. H. Leung and S. Yang, *Energy Environ. Sci.*, 2017, **10**, 593–603.

6 J. D. Benck, Z. Chen, L. Y. Kuritzky, A. J. Forman and T. F. Jaramillo, *ACS Catal.*, 2012, **2**, 1916–1923.

7 K. Chang, X. Hai, H. Pang, H. Zhang, L. Shi, G. Liu, H. Liu, G. Zhao, M. Li and J. Ye, *Adv. Mater.*, 2016, **28**, 10033–10041.

8 F. Wang, J. Li, F. Wang, T. A. Shifa, Z. Cheng, Z. Wang, K. Xu, X. Zhan, Q. Wang, Y. Huang, C. Jiang and J. He, *Adv. Funct. Mater.*, 2015, **25**, 6077–6083.

9 C. G. Morales-Guio, L.-A. Stern and X. Hu, *Chem. Soc. Rev.*, 2014, **43**, 6555–6569.

10 J. K. Norskov, T. Bligaard, J. Rossmeisl and C. H. Christensen, *Nat. Chem.*, 2009, **1**, 37–46.

11 Q. Lu, Y. Yu, Q. Ma, B. Chen and H. Zhang, *Adv. Mater.*, 2016, **28**, 1917–1933.

12 Z. W. Seh, J. Kibsgaard, C. F. Dickens, I. Chorkendorff, J. K. Norskov and T. F. Jaramillo, *Science*, 2017, **355**, eaad4998.

13 J. Kibsgaard, Z. Chen, B. N. Reinecke and T. F. Jaramillo, *Nat. Mater.*, 2012, **11**, 963–969.

14 X. Zhao, X. Ma, J. Sun, D. Li and X. Yang, *ACS Nano*, 2016, **10**, 2159–2166.

15 H. Li, C. Tsai, A. L. Koh, L. Cai, A. W. Contryman, A. H. Fragapane, J. Zhao, H. S. Han, H. C. Manoharan, F. Abild-Pedersen, J. K. Nørskov and X. Zheng, *Nat. Mater.*, 2015, **15**, 48–53.

16 G. Ye, Y. Gong, J. Lin, B. Li, Y. He, S. T. Pantelides, W. Zhou, R. Vajtai and P. M. Ajayan, *Nano Lett.*, 2016, **16**, 1097–1103.

17 T. F. Jaramillo, K. P. Jørgensen, J. Bonde, J. H. Nielsen, S. Horch and I. Chorkendorff, *Science*, 2007, **317**, 100–102.

18 H. Wang, H. Yuan, S. S. Hong, Y. Li and Y. Cui, *Chem. Soc. Rev.*, 2015, **44**, 2664–2680.

19 Y.-R. An, X.-L. Fan, Z.-F. Luo and W.-M. Lau, *Nano Lett.*, 2016, **17**, 368–376.

20 Y. Yang, H. Fei, G. Ruan, Y. Li and J. M. Tour, *Adv. Funct. Mater.*, 2015, **25**, 6199–6204.

21 C. Tsai, H. Li, S. Park, J. Park, H. S. Han, J. K. Norskov, X. Zheng and F. Abild-Pedersen, *Nat. Commun.*, 2017, **8**, 15113.

22 C.-C. Cheng, A.-Y. Lu, C.-C. Tseng, X. Yang, M. N. Hedhili, M.-C. Chen, K.-H. Wei and L.-J. Li, *Nano Energy*, 2016, **30**, 846–852.

23 J. M. Woods, Y. Jung, Y. Xie, W. Liu, Y. Liu, H. Wang and J. J. Cha, *ACS Nano*, 2016, **10**, 2004–2009.

24 H. Wang, Z. Lu, S. Xu, D. Kong, J. J. Cha, G. Zheng, P. C. Hsu, K. Yan, D. Bradshaw, F. B. Prinz and Y. Cui, *Proc. Natl. Acad. Sci. U. S. A.*, 2013, **110**, 19701–19706.

25 D. Kiriya, P. Lobaccaro, H. Y. Nyein, P. Taheri, M. Hettick, H. Shiraki, C. M. Sutter-Fella, P. Zhao, W. Gao, R. Maboudian, J. W. Ager and A. Javey, *Nano Lett.*, 2016, **16**, 4047–4053.

26 Z. Wu, B. Fang, A. Bonakdarpour, A. Sun, D. P. Wilkinson and D. Wang, *Appl. Catal., B*, 2012, **125**, 59–66.

27 L. Wu, N. Y. Dzade, L. Gao, D. O. Scanlon, Z. Ozturk, N. Hollingsworth, B. M. Weckhuysen, E. J. Hensen, N. H. de Leeuw and J. P. Hofmann, *Adv. Mater.*, 2016, **28**, 9602–9607.

28 G. J. A. Mannie, J. van Deelen, J. W. Niemantsverdriet and P. C. Thüne, *Appl. Phys. Lett.*, 2011, **98**, 051907.

29 G. J. A. Mannie, J. van Deelen, J. W. Niemantsverdriet and P. C. Thüne, *Appl. Surf. Sci.*, 2014, **309**, 263–270.

6078 | *Phys. Chem. Chem. Phys.*, 2019, **21**, 6071–6079

This journal is © the Owner Societies 2019

30 E. Erasmus, P. C. Thüne, M. W. G. M. Verhoeven, J. W. Niemantsverdriet and J. C. Swarts, *Catal. Commun.*, 2012, **27**, 193–199.

31 P. C. Thüne, C. J. Weststrate, P. Moodley, A. M. Saib, J. van de Loosdrecht, J. T. Millerc and J. W. Niemantsverdrieta, *Catal. Sci. Technol.*, 2011, **1**, 689–697.

32 Y. Jung, J. Shen, Y. Liu, J. M. Woods, Y. Sun and J. J. Cha, *Nano Lett.*, 2014, **14**, 6842–6849.

33 T. A. Loh, D. H. Chua and A. T. Wee, *Sci. Rep.*, 2015, **5**, 18116.

34 L. Ma, J. Peng, C. Wu, L. He and Y. Ni, *ACS Nano*, 2017, **11**, 2928–2933.

35 Y. D. Li, X. L. Li, R. R. He, J. Zhu and Z. X. Deng, *J. Am. Chem. Soc.*, 2002, **124**, 1411–1416.

36 S. M. Ng, H. F. Wong, W. C. Wong, C. K. Tan, S. Y. Choi, C. L. Mak, G. J. Li, Q. C. Dong and C. W. Leung, *Mater. Chem. Phys.*, 2016, **181**, 352–358.

37 L. Ma, Y. Hu, G. Zhu, R. Chen, T. Chen, H. Lu, Y. Wang, J. Liang, H. Liu, C. Yan, Z. Tie, Z. Jin and J. Liu, *Chem. Mater.*, 2016, **28**, 5733–5742.

38 F. Wang, P. He, Y. Li, T. A. Shifa, Y. Deng, K. Liu, Q. Wang, F. Wang, Y. Wen, Z. Wang, X. Zhan, L. Sun and J. He, *Adv. Funct. Mater.*, 2017, **27**, 1605802.

39 M. A. Pimenta, E. Del Corro, B. R. Carvalho, C. Fantini and L. M. Malard, *Acc. Chem. Res.*, 2015, **48**, 41–47.

40 A. Berkdemir, H. R. Gutiérrez, A. R. Botello-Méndez, N. Perea-López, A. L. Elías, C.-I. Chia, B. Wang, V. H. Crespi, F. López-Urías, J.-C. Charlier, H. Terrones and M. Terrones, *Sci. Rep.*, 2013, **3**, 1755.

41 A. Molina-Sánchez and L. Wirtz, *Phys. Rev. B: Condens. Matter Mater. Phys.*, 2011, **84**, 155413.

42 A. P. S. Gaur, S. Sahoo, M. Ahmadi, M. J. F. Guinel, S. K. Gupta, R. Pandey, S. K. Dey and R. S. Katiyar, *J. Phys. Chem. C*, 2013, **117**, 26262–26268.

43 Y. Li, H. Wang, L. Xie, Y. Liang, G. Hong and H. Dai, *J. Am. Chem. Soc.*, 2011, **133**, 7296–7299.

44 D. Voiry, H. Yamaguchi, J. Li, R. Silva, D. C. B. Alves, T. Fujita, M. Chen, T. Asefa, V. B. Shenoy, G. Eda and M. Chhowalla, *Nat. Mater.*, 2013, **12**, 850–855.

45 J. Yang, D. Voiry, S. J. Ahn, D. Kang, A. Y. Kim, M. Chhowalla and H. S. Shin, *Angew. Chem., Int. Ed.*, 2013, **52**, 13751–13754.

46 L. Cheng, W. Huang, Q. Gong, C. Liu, Z. Liu, Y. Li and H. Dai, *Angew. Chem., Int. Ed.*, 2014, **53**, 7860–7863.

47 J. Duan, S. Chen, B. A. Chambers, G. G. Andersson and S. Z. Qiao, *Adv. Mater.*, 2015, **27**, 4234–4241.

48 F. Wang, C. Di Valentin and G. Pacchioni, *J. Phys. Chem. C*, 2012, **116**, 10672–10679.

49 T. Zheng, W. Sang, Z. He, Q. Wei, B. Chen, H. Li, C. Cao, R. Huang, X. Yan, B. Pan, S. Zhou and J. Zeng, *Nano Lett.*, 2017, **17**, 7968–7973.

50 S. Bothra, H. Sur and V. Liang, *Microelectron. Reliab.*, 1999, **39**, 59–68.

This journal is © the Owner Societies 2019

Phys. Chem. Chem. Phys., 2019, **21**, 6071–6079 | 6079